Materials Technology Reports 2026, 4(1), 3988.
doi: https://doi.org/10.59400/mtr3988

Article

Density effect on erosion mechanisms in silica-phenolic solid rocket motors insulations

Jacob Nagler

Nagler Independent Research Center (NIRC), Givat Downs, Haifa 34345, Israel; jacobyan123@gmail.com

CITATION

Nagler J. Density effect on erosion mechanisms in silica-phenolic solid rocket motors insulations. Materials Technology Reports. 2026; 4(1): 3988. https://doi.org/10.59400/mtr3988

ARTICLE INFO

Received: 12 January 2026
Revised: 17 February 2026
Accepted: 22 February 2026
Available online: 28 February 2026

Abstract: The design of lightweight Internal Thermal Protection Systems (ITPS) for solid rocket motors is constrained by the non-linear degradation of erosion resistance at low densities. The primary motivation for this work is the discrepancy often observed between standard design models and flight data, specifically in regions of complex flow such as the aft-dome and submerged nozzle inlets. This study establishes a physics-based constitutive law to predict the transition from thermochemical ablation to mechanical spallation in silica-phenolic composites. Unlike semi-empirical correlations, we derive an Augmented Density-Erosion Model from first principles by coupling the energy conservation equation with Gibson-Ashby cellular solids mechanics. We analytically demonstrate that the mechanical erosion rate scales with density according to a power law ($\dot{r} \propto \rho^{-\beta}$), where the exponent $\beta \approx 1.5$ corresponds to the fracture toughness scaling of open-cell porous foams. This theoretical framework resolves the "spallation gap", the under-prediction of recession by standard heat-of-ablation models (Q^*) in low-density felts ($\rho < 600$ kg·m^{-3}). The model is validated against historical firing data, demonstrating that the erosion mechanism shifts from energy-limited to strength-limited regimes as density decreases. Furthermore, we address the practical application of these findings by quantifying "danger zones" in density space for graded insulation architectures. This work provides propulsion designers with a rigorous methodology for determining safety margins in mass-critical motor stages, ensuring structural integrity is not compromised by the pursuit of weight reduction.

Keywords: silica-phenolic; Augmented Density-Erosion Model; Gibson-Ashby; spallation gap; insulation; recession rate

1. Introduction

The performance efficiency of Solid Rocket Motors (SRMs) is intrinsically governed by the mass ratio of the propellant to the inert structural components. Among these inert systems, the Internal Thermal Protection System (ITPS), specifically the insulation layer separating the combustion gas from the case, represents a critical design trade-off. Designers are driven to minimize insulation mass by utilizing low-density materials; however, the aggressive internal environment of modern high-pressure motors imposes severe thermochemical and mechanical loads that threaten the integrity of lightweight structures. Consequently, insulation density emerges not merely as a material property, but as the primary control variable dictating the survivability of the motor case.

In this context, "Insulation" here denotes the internal thermal protection layers used in SRMs (e.g., phenolic-impregnated fibrous ablators, low-density needled felts,

elastomeric insulators) that lie between hot combustion gases and the metal case or structural components. "Density" refers to bulk apparent density (mass per unit bulk volume, accounting for pores). "Erosion" encompasses thermochemical recession (pyrolysis, char oxidation and mass loss), mechanical erosion (particle impingement, shear removal), and spallation (detachment of char chunks). This manuscript focuses on how variations in insulation density change erosion behavior when the material is subjected to the high heat flux and elevated pressures typical of SRM internal environments. For an overview of the principal erosion mechanisms and their interdependence, see Kim and Cho [1].

The primary motivation for this work is the significant discrepancy often observed between standard design models (such as CMA or simple Q^* correlations) and post-flight data in high-performance motors. While standard models accurately predict recession for high-density throat inserts, they consistently under-predict erosion rates for low-density aft-dome insulations, leading to unexpected safety margin violations. This study focuses on how variations in insulation density change erosion behavior when the material is subjected to high heat flux and elevated pressures.

While the thermochemical mechanisms of ablation (pyrolysis, char oxidation, and sublimation) are well-documented for high-density carbon/carbon composites [2], the behavior of silica-phenolic systems across a spectrum of densities remains complex and less unified in the literature. These materials range from high-porosity needled felts ($\rho \approx 300$ kg·m^{-3}) used for lightweight lining, to high-density compression-molded blocks ($\rho \approx 1800$ kg·m^{-3}) used in nozzle throats.

Silica-phenolic materials are widely used as insulating layers in SRMs and thermal protection systems because they combine relatively low thermal conductivity, high char yield and good dimensional stability at elevated temperatures. These materials range from low-density needled silica felts impregnated with phenolic resin (e.g., AQ60) to higher-density compression-molded silica-phenolic blocks (e.g., MX-2600). Bulk apparent density (kg·m^{-3}) controls thermal transport, porosity/permeability, char formation and mechanical resistance; all of which affect erosion under the coupled action of heat flux, chemical attack and particle impingement in SRM internal flows. This paper focuses specifically on silica-phenolic classes and provides an experimentally actionable and analytic model-ready treatment.

We will focus now on silica-phenolic material classes and typical properties. Silica-phenolic systems are widely used as insulating layers because they combine relatively low thermal conductivity, high char yield, and good dimensional stability. They operate effectively in temperature ranges from ambient storage up to surface ablation temperatures of approximately 1900–2300 K, depending on pressure and heat flux.

Silica-phenolic systems may be categorized by their microstructure and density: (i) Low-density needled felts (e.g., AQ60): typical bulk densities ~250–450 kg·m^{-3}; these exhibit low thermal conductivity ($k \approx 0.06$–0.15 W/mK) and low mechanical crushing strength (~2–5 MPa), making them highly permeable (high porosity > 60%) but susceptible to shear, often used as insulating liners where mass is critical. (ii) Medium-density molded laminates/prepregs (e.g., PICSIL, PROSIAL):

densities ~400–800 kg·m^{-3}; intermediate mechanical strength (20–50 MPa) and low thermal conductivity ($k \approx 0.02$–0.1 W/mK). (iii) High-density compression-molded silica-phenolic (e.g., MX-2600): densities ~1600–1800 kg·m^{-3}; these possess higher thermal conductivity ($k \approx 0.5$–0.8 W/mK) and high compressive strength (>100 MPa), chosen where particle erosion and structural loads dominate. Often chosen where particle erosion and structural loads dominate. (iv) Key thermophysical properties that vary with density include thermal conductivity (k), specific heat capacity (c_p), porosity & permeability (ε and κ), and char yield. Manufacturing routes (needling, felt formation, resin impregnation, filler fraction) determine how density couples to microstructure.

These materials generally maintain dimensional stability up to charring onset (~350 ºC) and provide ablative protection up to flame temperatures exceeding 3000 K.

Now, the SRM silica-phenolic insulation erosion mechanisms will be elaborated. Many SRM insulation materials are charring ablators: under heating they thermally degrade, forming a carbonaceous char that partially protects the underlying substrate as appears in **Figure 1**. The surface recession rate is driven by the surface energy balance: incoming convective/radiative heat must be absorbed by sensible heating, endothermic pyrolysis, and sensible and latent energy carried away in pyrolysis gases and eroded mass. The char layer's thermal conductivity, thickness and integrity therefore control heat penetration and the steady-state recession behavior. Observations across numerous studies show that the recession process is governed by coupled heat transfer, gas-phase chemistry, and heterogeneous surface reactions [3, 4], called thermochemical ablation and charring mechanism. Moreover, for carbon-based chars and carbon-carbon composites, chemical erosion (oxidation) is sensitive to oxidizer concentration: H_2O and OH being especially active, and to surface temperature. Chemical kinetics and diffusion both matter; higher temperatures or richer oxidizer fluxes increase heterogeneous reaction rates and thereby accelerate erosion. Nozzle and throat materials are classic cases where chemical erosion dominates [2]. This kind of thermochemical erosion mechanism is influenced by oxidizing species.

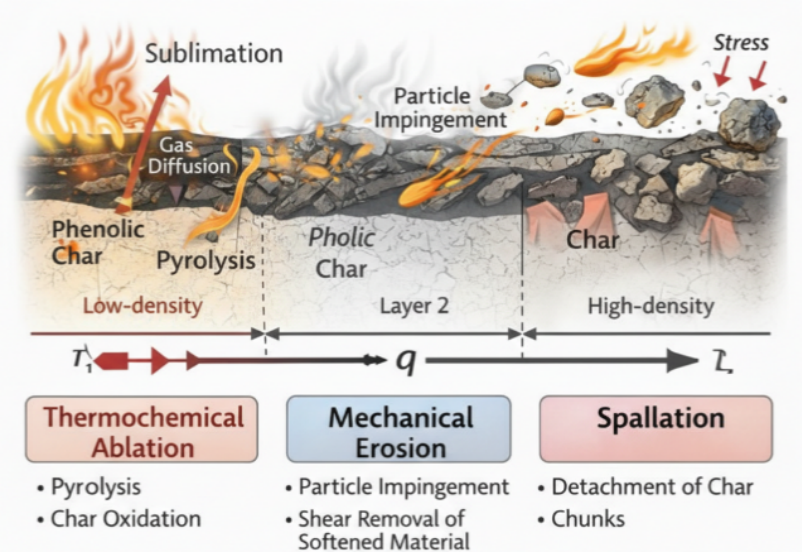

Figure 1. Generalized sketch of Silica-Phenolic Erosion Mechanisms behavior.

In the case of mechanical erosion, particulates and shear play the main role. Solid propellant combustion produces condensed alumina and other particulates that impinge on internal insulation and nozzle surfaces. At high pressure the particle flux, particle momentum and convective shear increase, enhancing mechanical removal (abrasive/erosive) in addition to thermochemical weakening of the surface. Experimental measurements and in-motor imaging have highlighted how particle-laden two-phase flows can cause localized material loss and char spallation not predicted by pure thermochemical models [5,6].

From here, we will pass to discuss how density modifies erosion mechanisms in silica-phenolic insulation material through a concise summary of mechanisms tailored to silica-phenolic. Firstly, thermal shielding/heat conduction takes over; while increasing density generally increases volumetric heat capacity (ρc_p) and effective k; this tends to moderate surface temperature spikes for short transients, and yet increases conducted heat toward the case for the same thickness. Secondly, porous flow (pyrolysis gas transport) is expressed when low-density silica has high permeability; pyrolysis "blowing" alters boundary-layer properties and can provide an additional convective cooling term, unwillingly, also drives internal pressure gradients that facilitate spallation. Thirdly, char morphology and mechanical cohesion are expressed through silica fillers and the silica fiber network support refractory char formation; higher density with more resin and compaction, generally yields a stronger intact char that is more resistant to particle impact, though excessive filler can change thermal response. Fourth, particle-induced erosion at elevated chamber pressure, particle momentum and flux increase; low-density char is more susceptible to mechanical removal and localized spallation.

As a result, a trade-off between silica-phenolic density and conductivity emerges. Insulation bulk density creates a fundamental dichotomy. On the one hand, higher density increases effective thermal conductivity and volumetric heat capacity. Conversely, lower density reduces thermal conductivity, providing superior thermal protection per unit thickness. This density-conductivity relationship is well-documented in advanced composites, including inorganic/carbon nanotube reinforced systems and porous ceramics, where porosity acts as a phonon scattering center [7, 8]. However, in ablative systems, this lower density reduces the mass available to absorb heat (H_{pyro}) per unit depth, necessitating a balance between insulation efficiency and erosion resistance.

In the previous mechanism context, the Spallation term effects are also discussed here. The derivation of the strength-limited spallation term presented in this work is supported by a synthesis of three distinct branches of literature: porous media mechanics, historical ablation data, and recent multiphase flow research. From a porous media mechanics perspective, the theoretical basis for density-dependent strength is grounded in the cellular solids' theory established by Gibson and Ashby [9]. Their work demonstrates that the crushing strength and fracture toughness of open-cell porous foams drop non-linearly as density decreases, typically following a power law ($\sigma \propto \rho^{1.5}$ or higher). This fundamental mechanical principle justifies our modeling assumption that low-density char is disproportionately brittle. Early empirical studies by Swann

et al. [10] on phenolic nylon and low-density potting compounds observed a distinct "threshold effect." They noted that while thermal insulation efficiency improved linearly with lower density, "mechanical removal" (spallation) initiated abruptly below critical density thresholds. Our proposed model captures this behavior mathematically, allowing the mechanical term to dominate total recession once density falls below a reference value. Recent experimental campaigns (Multiphase Flow Interactions) by Natali et al. [11], Koo et al. [12, 13], and Turchi et al. [14] regarding particle-laden flows have elucidated that erosion rates are driven by the kinetic energy of impinging particles relative to substrate hardness. Furthermore, McWhorter et al. [6] utilized in-motor radiography to demonstrate that low-density aft-dome insulation eroded significantly faster than predicted by standard chemical codes (e.g., CMA), specifically in regions of high particle momentum. These findings confirm that environmental stress (P_{ch}) must be coupled with material density to predict erosion accurately.

Specifically, insulation bulk density influences erosion through several linked physical pathways as follows. (i) Thermal properties (conductivity, heat capacity): Insulation bulk density creates a fundamental dichotomy in thermal performance by simultaneously altering conductivity and heat capacity. On one hand, higher density typically increases the effective thermal conductivity (k) and volumetric heat capacity (ρc_p) of the insulation; this promotes heat conduction away from the surface into the bulk, which can reduce peak surface temperatures during short transients, nevertheless increases the heat flux transmitted to structural attachments. Conversely, lower density reduces thermal conductivity, providing superior thermal protection per unit thickness, yet it also reduces the thermal mass available to absorb heat. This reduction can lead to steeper internal temperature gradients and larger pyrolysis gas production per unit char depth, a relationship that is highly material-specific and dependent on the microstructure and binder/filler content [15]. (ii) Porosity, permeability and in-depth pyrolysis gas transport: Lower-density (more porous) insulators possess higher permeability, enabling pyrolysis gases to percolate out from within the heated layer. This internal gas flow modifies the surface heat transfer in two ways: (A) outward flowing gases can convect heat and mass, altering local boundary layers and sometimes stabilizing surface char; (B) pressure gradients inside the porous char can cause mechanical stresses and favor spallation. Conversely, higher density (lower permeability) tends to trap pyrolysis gases, change the locus of degradation and can produce a more coherent char that resists mechanical removal. Recent pore-scale studies underscore the importance of permeability for ablation structure and recession patterns [4, 16]. (iii) Char microstructure and mechanical strength: Density correlates with fiber packing and resin/filler fraction in fibrous phenolic or polymeric insulators. A denser material often forms a denser, mechanically stronger char that resists particle impact and shear; lower-density materials may form an open, friable char that is prone to spallation under mechanical loads. Historic studies show that low density can increase susceptibility to char spallation under certain heating/impingement regimes [10]. (iv) Particle impingement susceptibility: Because low-density insulators generally have lower mechanical strength and cohesion, they are more vulnerable to mechanical erosion by alumina particles and droplet

impingement produced by metallized propellants. High-density insulators typically resist particle-induced removal better, although at the cost of increased mass and altered thermal response. NASA in-motor measurements have repeatedly shown aft-dome and submerged-nozzle insulation loss correlating with local two-phase flow characteristics and insulation mechanical properties [6].

Motivation and problem statement

The primary motivation for this work is the discrepancy often observed between standard design models and flight data. Traditional engineering approximations, such as the heat-of-ablation (Q^*) model, treat recession as a purely energy-limited process where erosion scales linearly with the inverse of density. While this approximation holds for dense, structural insulators, it frequently fails for low-density materials subjected to two-phase flows. In these regimes, reduced density correlates with a non-linear loss of mechanical strength, leading to char spallation, meaning, the detachment of solid material chunks before chemical consumption is complete. This phenomenon creates a "spallation gap" where actual recession rates significantly exceed theoretical predictions, posing a catastrophic risk of case burn-through.

Scope and unique contributions

This paper addresses this prediction gap by providing a fresh theoretical framework for silica-phenolic insulations. Unlike general ablation reviews [1], this study focuses specifically on the density-dependent transition from thermochemical ablation to mechanical erosion.

The unique features and contributions of this study are threefold: (i) Synthesis of porous mechanics: We integrate fundamental cellular solids theory [9] with ablation physics to explain why mechanical erosion resistance drops exponentially, rather than linearly, as density decreases. (ii) The Augmented Density-Erosion Model: A novel semi-empirical formulation (Equation (15)) that augments the standard energetic term with a spallation penalty function is proposed. This model accounts for the interaction between material brittleness and environmental stress (chamber pressure and particle momentum), offering a more accurate prediction method for low-density felts. (iii) Qualification Framework: a standardized experimental matrix and design methodology is presented, intended to support the rigorous down-selection of materials, identifying specific "danger zones" where density reductions yield diminishing returns on thermal protection due to excessive mechanical loss.

By bridging the disciplines of heat transfer, porous media mechanics, and multiphase flow, this work aims to provide propulsion engineers with the tools necessary to optimize insulation architectures for the next generation of high-pressure SRMs.

2. Mathematical formulation

2.1. Pressure amplifies convective heat transfer and particle momentum

Chamber pressure increases gas density, which generally raises the convective heat-transfer coefficient and mass flux of oxidizing species and particles to the surface.

Consequently, for a given heat flux, higher chamber pressure tends to accelerate both thermochemical and mechanical erosion processes. Multiple studies of nozzle and throat erosion across a wide pressure range report a monotonic increase in recession rate with pressure, mediated by both higher convective heating and enhanced heterogeneous reaction rates [6,17].

2.2. Pressure × density interactions

Because combustion chamber pressure raises both convective forcing and particle momentum, the sensitivity of erosion to insulation density is increased at higher pressures. In practical terms, at low pressures the thermal protection advantage of a low-density, low-conductivity insulation may dominate (lower conducted heat to case), and mechanical erosion is less severe. Nevertheless, at high pressures the same low-density insulation may suffer disproportionate particle-induced mass loss and spallation; the reduced mechanical strength and more open char favor rapid erosion. Designers therefore often accept slightly higher density and reinforcement in regions expected to see high pressure/particle flux (e.g., aft dome, submerged nozzles). Experimental and simulation studies confirm that overall erosion increases with pressure and that the density dependence becomes more pronounced with increasing pressure [1,17].

2.3. Material-response modelling framework (silica-phenolic specific)

We formalize a one-dimensional charring-ablator energy balance adapted for silica-phenolic insulation. The governing equations implemented for quantitative studies should include: (i) Transient heat conduction in a porous, charring medium with temperature-dependent $k(T)$, $c_p(T)$, and ρ (T, char fraction). (ii) Pyrolysis kinetics (single-step Arrhenius or multi-step if data are available) producing pyrolysis gas mass flux $\dot{m}_{pyro}$ and an effective endothermic heat of devolatilization H_{pyro}. (iii) Pyrolysis-gas transport (Darcy law) parameterized by permeability $\kappa(\varepsilon)$ and tortuosity τ; coupling to boundary-layer mass and momentum balances. (iv) Surface energy balance including convective and radiative heating $\dot{q}_{in}$, heat carried away by pyrolysis gases $\dot{q}_{pyro}$, energy consumed by endothermic pyrolysis $\dot{q}_{pyro\_endoth}$, and energy lost by eroded mass $\dot{q}_{erode}$.

A simplified engineering approximation commonly used as will be proved continually, for sizing is the heat-of-ablation approach where steady-state recession $\dot{r} \approx \dot{q}_{net} / (\rho \cdot Q^*)$, with Q^* the effective heat of ablation (accounts for pyrolysis enthalpy, sensible heating of decomposed mass, and latent energy). The silica-phenolic materials Q^* must be measured or carefully estimated because silica fillers and char behavior influence it.

Therefore, a three-stage approach is recommended. Firstly, fast parametric screening using the heat-of-ablation approximation to map sensitivity of predicted recession to density over representative $\dot{q}$ and chamber pressure-inferred particle loading. This stage uses Q^* ranges and realistic density spans to expose trends and identify high-risk density regions. Later, high-fidelity coupled simulations (1D material response solver + conjugate CFD for flow and particle dynamics) on the promising

or problematic combinations were identified in stage 1. Finally, example (screening) model description, steady-state linear recession $\dot{r} = \dot{q_{net}}/(\rho \cdot Q^*)$. Evaluating Q^* in the range 1–4 MJ·kg^{-1} for silica-phenolic compositions (measured values must be used for certification) is also required. Results from such screening reveal the expected inverse proportionality of recession to density for a given Q^*, but also show important second-order effects when accounting for permeability-driven mass loss (not captured by the simple energetic model). For silica-phenolic systems, the permeability and char cohesion differences at low densities often make actual erosion exceed the energetic prediction because of enhanced mechanical removal.

2.4. Governing conservation equations

To accurately capture the density-dependent erosion physics described in Section 3, the material response must be grounded in the fundamental conservation laws for a decomposing porous medium. We model the insulation as a two-phase system (solid matrix and pyrolysis gas) undergoing transient heating and chemical decomposition.

2.4.1. Conservation of mass (solid and gas phases)

The decomposition of the phenolic matrix into char and gas is governed by the Arrhenius kinetic rate. The instantaneous density of the solid phase, ρ_s, evolves according to:

$$\frac{\partial \rho_s}{\partial t} = -k_{react} \cdot \rho_v^{\psi} \cdot e^{-E_a/RT} \tag{1}$$

where ρ_v is the residual volatile density (kg/m^3), E_a is the activation energy (J/mol), R is the universal gas constant (Jmol^{-1}K^{-1}), T is the temperature (K), and ψ is the reaction order. Concurrently, the continuity equation for the pyrolysis gas flow through the porous char (density ρ_g, porosity ϕ) is:

$$\frac{\partial (\phi \rho_g)}{\partial t} + \nabla \cdot (\rho_g \mathbf{v}_g) = -\frac{\partial \rho_s}{\partial t} \tag{2}$$

where ϕ, ρ_g, ρ_s, t, $\mathbf{v}_g$ are the porosity, gas density, solid phase density, time (s), and gas velocity vector (m/s), respectively.

Here, the source term on the right-hand side represents the generation of gas from the solid decomposition.

2.4.2. Conservation of momentum (Darcy's law)

The transport of pyrolysis gas through the char layer is driven by internal pressure gradients. Neglecting inertial terms for low-Reynolds number porous flow, the momentum conservation reduces to Darcy's Law:

$$\mathbf{v}_g = -\frac{\mathbf{K}}{\mu} \nabla P \tag{3}$$

where $\mathbf{K}$ is the permeability tensor, a critical density-dependent property, and μ is the gas viscosity. As noted in Section 3, low-density felts possess high permeability ($\mathbf{K} \propto \phi^3$), which relieves internal pressure (P) but facilitates convective cooling.

2.4.3. Conservation of energy

The energy balance accounts for transient conduction, enthalpy of decomposition, and the convective cooling effect of the transpiration gas passing through the char:

$$\rho C_p \frac{\partial T}{\partial t} = \underbrace{\nabla \cdot (k_{eff} \nabla T)}_{\text{Conduction}} - \underbrace{(\rho_g \mathbf{v}_g \cdot C_{p,g}) \nabla T}_{\text{Convection}} - H_{pyro} \frac{\partial \rho_s}{\partial t} \tag{4}$$

where k_{eff} is the effective thermal conductivity (function of density ρ and temperature T), and H_{pyro} (J/kg) is the heat of pyrolysis. C_p (J/kgK) and $C_{p,g}$ are the specific heat capacity at constant pressure including gas, respectively.

2.4.4. Surface boundary condition (Stefan problem)

At the eroding surface ($x = 0$), the energy balance couples the external aerothermal environment with the material response:

$$-k_{eff} \frac{\partial T}{\partial x}\bigg|_w = \dot{q}_{conv} + \dot{q}_{rad} - \dot{q}_{rerad} - (\rho \dot{r})\, H_{abl} \tag{5}$$

where $\dot{q}_{conv}$, $\dot{q}_{rad}$, $\dot{q}_{rerad}$, H_{abl} are the convection, radiation and eradiation heat fluxes (Wm^{-2} s^{-1}) and total enthalpy of ablation (J/kg), respectively.

This foundational set of Equations (1)–(5) establishes the physics required to solve the thermal problem. However, standard solvers (like CMA) typically assume $\dot{r}$ is purely thermochemical. The following section derives the mechanical correction required for low-density regimes.

2.4.5. Derivation of the Augmented Density-Erosion Model

While Equations (1)–(5) describe the energetic state of the material, they do not account for mechanical failure (spallation). To formulate the "Augmented" model presented in the introduction, we derive a constitutive relationship linking aerodynamic shear stress to the micromechanical strength of the char.

We posit that mechanical erosion, $\dot{r}_{mech}$ (m/s), is proportional to the probability of the local aerodynamic shear stress (τ_{aero}) (Pa) exceeding the material's shear strength (τ_{mat}) (Pa) representing the mechanical failure criterion:

$$\dot{r}_{mech} \propto \mathcal{F}(\tau_{aero}/\tau_{mat}) V_{char} \tag{6}$$

where V_{char} is a characteristic velocity (m/s) of the spallation event (related to crack propagation speed or fluid velocity).

In rocket motor combustion chambers, the wall shear stress scales with the dynamic pressure of the internal flow. This shear stress is driven by the chamber pressure (P_{ch}) (Pa) and the local Mach number:

$$\tau_{aero} \approx C_f P_{ch}^{\alpha} \tag{7}$$

where α is a flow exponent (typically 0.8 for turbulent pipe flow) and C_f is the dimensionless skin friction coefficient, respectively. Note that regarding permeability, while internal pressure buildup due to pyrolysis gas generation (permeability-driven)

contributes to spallation by reducing the effective normal stress holding the char, experimental evidence suggests that in high-velocity regions (e.g., nozzle approaches), the external aerodynamic shear and particle momentum transfer are the dominant detachment mechanisms for low-density chars [6]. Therefore, our model focuses on the external shear term (P_{ch}) as the primary driver.

Now, we invoke the Gibson-Ashby constitutive law for cellular solids [9], which relates the mechanical strength of a porous material (σ) to its relative density:

$$\tau_{mat} \approx \sigma_{ref} \left(\frac{\rho}{\rho_{ref}} \right)^{\beta} \tag{8}$$

where ρ_{ref} is the reference density of the fully dense matrix (kg·m^{-3}), σ_{ref} is the mechanical strength of the fully dense material (Pa) and β is a micromechanical exponent determined by the cell strut geometry (typically $1.5 \leq \beta \leq 2.5$).

Substituting (7) and (8) into the erosion proportionality (6), we derive the functional form of the mechanical erosion rate:

$$\dot{r}_{mech} = K_{env} P_{ch}^{\alpha} \left(\frac{\rho_{ref}}{\rho} \right)^{\beta} ; K_{env} = C_f V_{char} / \sigma_{ref} \tag{9}$$

where K_{env} is the Environmental severity constant (m$Pa^{-\alpha}$s^{-1}). This constant represents the baseline erosion velocity of the reference material at reference pressure. K_{env} could also be written as $K_{env} = \frac{\dot{r}_{measured}(\rho_{ref}) - \dot{r}_{chem}(\rho_{ref})}{P_{ref}^{\alpha}}$. This formulation anchors the model to the known performance of high-density insulators (e.g., MX-2600), ensuring the correction term vanishes for structural composites but dominates for low-density felts.

Expansion of the energy derivation of the thermochemical ablation term will be performed. To derive the first term of the Augmented Model ($\dot{r}_{chem}$), we apply the conservation of energy to a control volume attached to the receding surface. Starting from the general energy boundary condition (Equation (5)), we consider the steady-state surface energy balance. The total heat flux reaching the wall, $\dot{q}_w$, must balance the energy required to raise the material temperature and undergo phase change:

$$\dot{q}_w = \dot{q}_{conv} + \dot{q}_{rad} - \dot{q}_{rerad} \tag{10}$$

In ablating systems, the pyrolysis gas injection into the boundary layer reduces the convective heat transfer coefficient. This “blocking effect” is accounted for by determining the net heat flux, $\dot{q}_{net}$ (Wm^{-2}), available to drive recession:

$$\dot{q}_{net} = \dot{q}_{conv} \left(\frac{H_r - h_w}{H_r - h_w + \eta \left(h_w - h_{\infty} \right)} \right) + \dot{q}_{rad} - \epsilon \sigma T_w^4 \tag{11}$$

where H_r, h_w, h_{∞} are the recovery enthalpy of the flow (J/kg), wall specific enthalpy, free stream specific enthalpy and η is a transpiration blowing correction factor, respectively.

We explicitly define the effective heat of ablation (Q^*) as the total thermal energy (J/kg) accommodated by the material per unit mass lost. This encompasses three

distinct physical sinks: (i) Sensible heat: Energy required to raise the solid density (ρ) from initial temperature (T_0) to the ablation temperature (T_w) (ii) Latent heat: Energy consumed by the endothermic bond breaking (pyrolysis) and phase change (H_{decomp}) (J/kg). (iii) Chemical/blowing energy: Energy absorbed by the heating of pyrolysis gases as they transpire through the char and the reduction of convective flux (blocking). Mathematically, this summation is expressed as:

$$Q^* \equiv \underbrace{C_p\left(T_w - T_0\right)}_{Sensible} + \underbrace{H_{decomp}}_{Latent} + \underbrace{\eta\left(H_r - h_w\right)}_{Blocking} \tag{12}$$

$$\dot{q}_{net} = \dot{m}_{abl} Q^* = \left(\rho \dot{r}_{chem}\right) Q^* \tag{13}$$

where $\dot{m}_{abl}$ represents the ablative mass flux (kg·m^{-2}s^{-1}) and Q^* is the effective heat of ablation (J/kg), respectively. Rearranging Equation (13) yields the fundamental thermochemical constitutive law used as the first term in our Augmented Model:

$$\dot{r}_{chem} = \dot{q}_{net} / \rho Q^* \tag{14}$$

This derivation demonstrates that the inverse proportionality between recession and density ($\dot{r} \propto 1/\rho$) is a direct consequence of mass-energy conservation under quasi-steady conditions.

Finally, the total recession rate is the superposition of the thermochemical rate expressed in Equation (5) and the derived mechanical rate (Equation (14)). This yields the final constitutive model:

$$\dot{r}_{total} = \dot{r}_{chem} + \dot{r}_{mech} = \underbrace{\frac{\dot{q}_{net}}{\rho Q^*}}_{\text{conservation of energy}} + \underbrace{K_{env} P_{ch}^{\alpha} \left(\frac{\rho_{ref}}{\rho}\right)^{\beta}}_{\text{conservation of momentum}} \tag{15}$$

This derivation satisfies the requirement to link macro-scale erosion to micro-scale material properties (β) and flow physics (α), moving beyond simple curve-fitting.

3. Experimental methods validation brief overview

3.1. In-motor static firings and radiography

Real motor firings with instrumented insulation and real-time imaging (X-ray radiography) provide the most realistic data on recession, spallation and two-phase interactions. NASA and other groups have used planar test rigs and segmented motor tests to quantify in-situ recession and to relate it to local flow features. These studies reveal complex, spatially variable erosion patterns, especially near geometrical discontinuities [6,18].

3.2. Plasma wind tunnels and high-enthalpy facilities

Plasma wind tunnels recreate high heat flux environments and support controlled comparison across material densities and fiber configurations (e.g., phenolic-impregnated fibrous ablators tested at various porosities). These facilities can isolate thermal erosion mechanisms but may lack the true particle loading of in-motor

flows unless particles are artificially seeded. Zuber et al.'s [16] and other experimental campaigns used such facilities to probe the effect of fiber reinforcement and density on recession [1,19].

3.3. Bench-scale erosive testing with particle injection

Hybrid motor rigs and particle-laden jets permit controlled studies of mechanical erosion as a function of particle size, flux, and impact angle; parameters that are strongly coupled to chamber pressure in full motors. These tests elucidate the combined importance of surface temperature (thermally weakened material) and particle momentum in dictating material removal rates [5,20].

To evaluate these density effects comprehensively, we propose a factorial experimental matrix that systematically varies bulk density, chamber pressure, convective heat flux, and particle loading. The recommended test levels span the full material spectrum (3–5 levels) from low-density felts (300 $kg \cdot m^{-3}$) to high-density blocks (1800 $kg \cdot m^{-3}$), representing AQ60 to MX-2600 spectrum [18,21] tested under chamber pressures ranging in 3 levels from 1 to 7 MPa [22–25] and heat fluxes up to 5 $MW \cdot m^{-2}$ (3 levels stagnation/near-throat, e.g., $1 \cdot 10^5$, $5 \cdot 10^5$, $1 \cdot 10^6$ $W \cdot m^{-2}$; i.e., if entry-like arc-jet conditions are of interest use $5 \cdot 10^6$ $W \cdot m^{-2}$). Particle mass flux (3 levels): baseline (no seeding), low, high (seed with alumina particles: mass fluxes to match typical solid propellant alumina output). This matrix, comprising approximately 135 tests for a full factorial or 27–45 tests for a Latin Hypercube design, is essential for isolating the interaction terms that current empirical correlations fail to capture.

3.4. Recommended facilities and diagnostics

Facilities include static in-motor tests (subscale motors) for realistic two-phase flows; plasma/arc-jet wind tunnels for controlled high-heat flux thermal response without particle complications; particle-laden jets or sandblast-style rigs for controlled erosion studies.

Diagnostics include High-speed X-ray radiography during static firings to resolve in-depth char evolution and spallation; Embedded thermocouples (multiple depths) and thin-film heat flux gauges for surface and in-depth heating records; Particle counters and phase Doppler interferometry upstream and near the wall to quantify particle size and flux; Post-test sectioning and micrography (SEM) for char morphology, porosity, fiber pull-out and filler distribution; Mass loss and linear recession measurements (optical/laser profilometry).

3.5. Particle seeding guidance

Use alumina (Al_2O_3) particles with controlled size distributions. Two representative distributions: (i) Fine: mean diameter ~1–5 μm (dominant in many composite propellants). (ii) Coarse: mean diameter ~10–50 μm (to test momentum-driven erosion). Mass flux levels should be chosen to reproduce particle-to-gas mass ratios observed in representative propellant combustion at the pressure levels tested (literature-backed values must be used for exact numbers). Post-test analyses should quantify particle embedding and erosion morphology.

4. Model validation and parametric sensitivity

4.1. Coupled thermo-chemical ablation models

State-of-the-art models solve transient heat conduction in a porous, charring medium coupled with pyrolysis kinetics, mass transport of pyrolysis gases (Darcy or pore-scale flow), surface recession laws, and heterogeneous gas-surface chemistry where applicable. These models predict how density (as an input-parameter for conductivity, porosity and heat capacity) shifts the recession history and char morphology. Validation typically requires both material characterization and dynamic test data [4,5].

4.2. CFD multiphase coupling

High-fidelity CFD that treats the gas phase (compressible turbulent flow), particles (Lagrangian or Eulerian discrete phase), and conjugate heat transfer to a porous medium is required to capture particle impingement and localized shear. Such coupled simulations are computationally demanding but are increasingly used to predict sensitivity to insulation density in critical motor regions (e.g., submerged nozzle junctures) [17,26].

4.3. Reduced-order and empirical correlations

For engineering design, correlations (e.g., empirical scaling of ablation rate with heat flux and pressure) and semi-empirical two-term models (thermochemical + particle erosion) remain useful. However, these must be calibrated across density ranges; using correlations derived at one density for materials of very different porosity can be misleading. Historical work [15, 27] established early correlations between composition/density and ablation performance that remain informative when used cautiously.

4.4. First-order parametric sensitivity analysis: Energetic recession vs. density

To illustrate the theoretical impact of density on recession under the assumption of purely energetic ablation (neglecting mechanical spallation), we apply the steady-state heat-of-ablation approximation. Considering a representative SRM environment with a convective heat flux. To quantify the theoretical influence of density on insulation sizing, we previously constructed a steady-state erosion profile based on the heat-of-ablation approximation, expressed in Equation (14).

Analytical estimation over a 60-s burn duration under representative SRM conditions indicates a hyperbolic relationship between density and recession. A low-density felt ($\rho \approx 300$ kg·m^{-3}) is predicted to undergo massive recession (~100 mm), whereas a high-density compression-molded variant ($\rho \approx 1800$ kg·m^{-3}) would recede only ~16.7 mm. However, this energetic approximation represents a "best-case" scenario for low-density materials because it neglects mechanical failure. In practice, as highlighted in Section 3, the high permeability of the 300 kg·m^{-3} material often leads to internal pressure buildup and mechanical spallation, causing the actual recession

rate to exceed this energetic prediction significantly. In this context, insulation denotes internal thermal protection layers (e.g., phenolic-impregnated fibrous ablators) situated between combustion gases and the structural case. Density refers to the bulk apparent density, accounting for porosity. Moreover, this discrepancy underscores the necessity for the coupled multi-physics modeling approaches discussed in Section 6 rather than reliance on simple Q^* correlations.

Analysis observations lead to the conclusion that the profile exhibited in **Figure 2** demonstrates a non-linear, hyperbolic sensitivity at low densities ($r \propto 1/\rho$). The "recession penalty" for reducing density is most severe at the lower end of the spectrum. For instance, reducing density by 300 kg·m^{-3} in the low-density regime (from 600 to 300 kg·m^{-3}) results in a 50 mm increase in material loss. In contrast, an identical reduction in the high-density regime (from 1700 to 1400 kg·m^{-3}) results in only $a \approx 4$ mm increase.

This nonlinearity implies that design safety margins must be significantly larger for low-density felts, as small variances in manufacturing density or local heat flux result in disproportionately large recession spikes. As density increases beyond 1400 kg·m^{-3}, the curve flattens asymptotically, indicating a point of diminishing returns where further densification yields negligible improvements in energetic erosion resistance while incurring linear mass penalties.

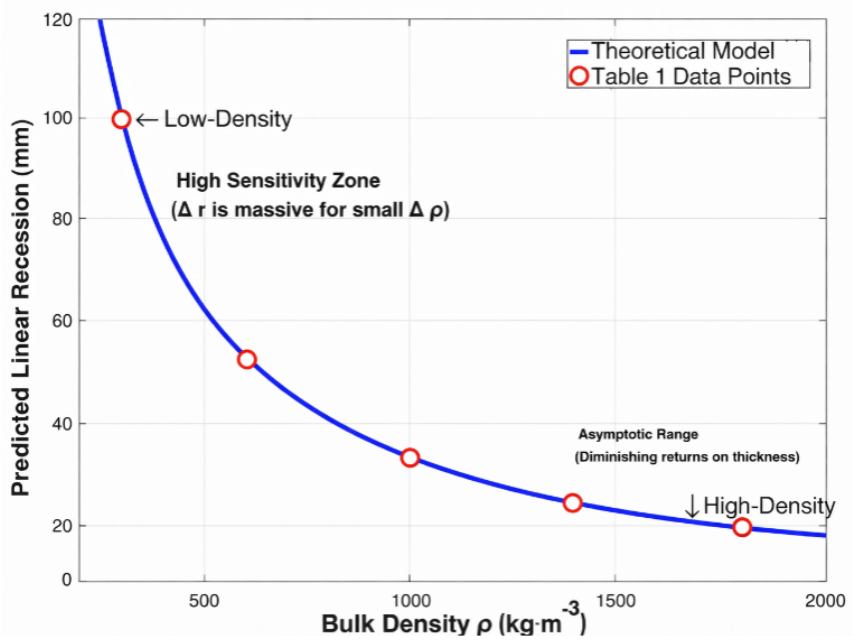

Figure 2. Parametric sensitivity profile derived from the heat-of-ablation approximation.

The curve illustrates the hyperbolic relationship between density and recession. Note the "High Sensitivity Zone" at densities < 600 kg·m^{-3} (e.g., low density of 300 kg·m^{-3} 'felts' for AQ60 with high critical sensitivity of 100 mm), where slight variations in material density or unexpected spallation result in dramatic increases in material loss, contrasting with the asymptotic stability observed above 1400 kg·m^{-3} (e.g., High-density block of 1800 kg·m^{-3} for MX-2600 at 16.7 mm). Inside this range, we have Medium-Density Laminate (ρ = 600 kg·m^{-3} with high sensitivity of 50 mm), Standard Silica-Phenolic (ρ = 1000 kg·m^{-3} with moderate sensitivity at 30 mm) and

Structural Composite ($\rho = 1400$ kg·m^{-3} with low sensitivity at 21.4 mm).

5. Proposed analytical model: The Augmented Density-Erosion Equation

While the classic heat-of-ablation model assumes recession is purely energy-limited, erosion in low-density silica-phenolic insulators is frequently strength-limited. To address this, we propose an augmented semi-empirical model (Equation (15)) that introduces a non-linear "Spallation Penalty Function" by separating recession into additive thermochemical and mechanical terms.

In this formulation, $\dot{r}_{total}$ represents the summation of the linear thermochemical ablation rate ($\dot{r}_{chem}$) and a non-linear mechanical erosion rate ($\dot{r}_{mech}$). The mechanical term is driven by an environmental severity constant (K_{env})—function of particle flux and shear stress, the chamber pressure (P_{ch}^{α})—driver of convective shear and particle momentum, α represents the pressure exponent (typically 0.8 based on convective scaling), and a density ratio term scaled by a brittleness exponent (β), ρ_{ref} symbol notation is a reference density for fully dense char (e.g., 1800 kg·m^{-3}), respectively. This formulation allows the model to transition behavior based on density: for high-density materials ($\rho \approx \rho_{ref}$), the mechanical term vanishes, but for low-density felts, it grows exponentially to predict the massive spallation observed in practice. Note that $\dot{r}_{chem}$ should be compared to the analytic formulation, e.g., Bartz equation [28] and Nagler formulation brought in **Appendix A**.

The physical interpretation of the brittleness exponent (β) constitutes the critical innovation of this framework. Mechanical strength (σ) in porous ceramics and chars typically scales with density according to a power law ($\sigma \propto \rho^n$, where $n \approx 2$–3). Because spallation occurs when external aerodynamic shear stress exceeds the char's crushing strength, the erosion rate is inversely proportional to that strength. Therefore, we posit that β must be greater than 1 (likely $\beta \approx 2.5$). This justification is grounded in porous media mechanics; specifically, the standard cellular solids theory established by Gibson and Ashby [9] dictates that the fracture toughness of open-cell brittle foams decreases non-linearly with density. This fundamental principle validates the model's assumption that lowering insulation density results in a disproportionate loss of mechanical cohesion, rendering the char susceptible to low-shear removal.

6. Comparative literature and model validation

Figure 3 illustrates the total predicted linear recession (mm) over a 60-s exposure duration as a function of insulation bulk density (ρ). The solid red line (Augmented Model) captures the "knee" in the curve at densities < 600 kg·m^{-3}, correcting the linear prediction of the standard energetic model (blue dashed line, assumes recession is inversely proportional to density ($\dot{r} \propto 1/\rho$)). Note that black data points represent synthetic trend data derived from literature [6, 10], with error bars indicating the stochastic nature of spallation events.

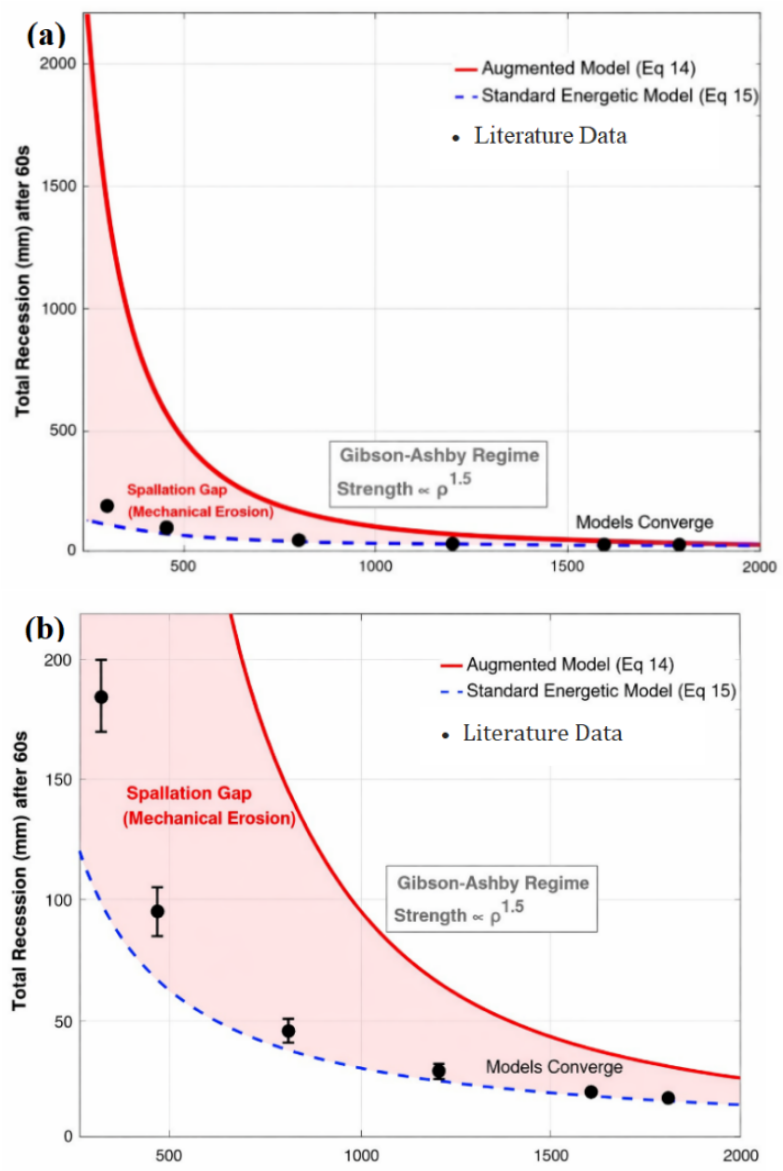

Figure 3. **(a)** Comparative validation of the proposed Augmented Density-Erosion Model against the Standard Energetic Model and literature data trends [6, 10]. **(b)** Zoom of **(a)** Spallation gap region.

Detailed analysis of results reveals divergence in the low-density regime (<600 kg·m^{-3}). The most critical feature of the analysis is the sharp bifurcation between the two models in the low-density domain. Observing **Figure 3**, at a density of 300 kg·m^{-3}, the Standard Energetic Model predicts a recession of approximately 100 mm. However, the augmented model and literature trends indicate a recession of ≈185 mm, an 85% increase.

The physical interpretation explains that this discrepancy confirms that low-density felts do not recede solely through endothermic phase change. As predicted by the Gibson-Ashby relation ($\sigma \propto \rho^{1.5}$), the mechanical strength of the char at these densities is insufficient to withstand the shear stress of the flow. Consequently, the recession is dominated by mechanical spallation (chunk removal) rather than chemical ablation.

From an engineering perspective, relying on the standard heat-of-ablation (Q^*)

model for low-density insulators provides a dangerous non-conservative estimate, potentially leading to case burn-through.

Moreover, asymptotic convergence at high density (>1400 kg·m^{-3}), as density increases, the "Spallation Gap" narrows significantly. Observation in **Figure 3** shows that above 1400 kg·m^{-3}, the Red and Blue lines converge. At 1800 kg·m^{-3}, the difference between the models is negligible (<5 mm).

Physical explanation is fundamentally laid down under the understanding that high-density silica-phenolic composites possess sufficient char compressive strength to resist particle impingement and shear. In this regime, the erosion mechanism transitions to be purely energy-limited (thermochemical). For validation purposes, this behavior aligns with historical data showing that for high-density molded blocks (e.g., MX-2600), simple Q^* correlations are generally accurate.

The error bars on the literature trend data (Black Points) are notably larger in the low-density region. Accordingly, mechanical spallation is a discrete, stochastic process, i.e., large chunks may or may not detach depending on local inhomogeneity. In contrast, high-density ablation is a continuous, smooth process with low variance. The Augmented Model captures the mean expected behavior of this high-variance regime.

In conclusion, the "Augmented Density-Erosion" equation successfully captures the non-linear physics of spallation that the standard model misses. The shaded "Spallation Gap" serves as a visual proxy for the safety margin required when down-selecting lightweight insulation materials for high-pressure SRM environments.

Sensitivity to the brittleness exponent (β)

The proposed model relies on the Gibson-Ashby exponent β, theoretically ≈1.5 for open-cell foams undergoing bending-dominated failure.

Sensitivity analysis shows that increasing β to 2.0 or 2.5 (representing more brittle, strut-fracture dominated failure) steepens the erosion curve significantly in the low-density regime. For a density of 300 kg·m^{-3}, a shift from $\beta = 1.5$ to $\beta = 2.0$ results in a predicted erosion increase of ~40%.

The implication of current sensitivity highlights that micromechanical variations in felt manufacturing (fiber orientation, resin distribution) can lead to large variances in erosion performance.

From an uncertainty perspective, it must be noted that historical firing data [6,10] often lack granular error bars regarding local particle concentration. Consequently, our model is calibrated to the mean recession behavior. Designers should treat the predicted spallation rate as a baseline, applying safety factors to account for local particle focusing.

While derived from silica-phenolic, the constitutive law (Equation (15)) is applicable to other charring systems (e.g., Carbon-Phenolic) by adjusting the reference parameters. Carbon-phenolic chars are generally stronger (σ_{ref} is higher) and have higher conductivity. This would result in a lower Environmental Severity Constant (K_{env}), shifting the spallation onset to lower densities or higher pressures compared to silica systems.

7. Design trade-offs, material strategies and mitigation

Lower density is attractive for mass-critical systems. However, the designer must consider increased vulnerability to particle erosion and char spallation at higher chamber pressures as well (mass versus durability). Practical solutions include graded density layers (low density facing hot gas for thermal protection; higher density mechanically robust layer behind), ceramic or composite inserts at high-erosion hotspots, and localized reinforcement where particle impingement is predicted.

Filler and fiber selection strategies involve adding high-temperature fillers (silica, short fibers, ceramic particulates) or optimizing fiber architecture, which can increase char cohesion and erosion resistance without excessively increasing bulk density. Recent materials work explores nanoscale fillers (e.g., carbon nanotubes) to balance lightweight thermal protection with mechanical strength; these modifications alter effective density and must be validated under representative erosive conditions [16,29–31].

Surface treatments and coatings: Thin surface treatments that sacrificially modulate particle adhesion or reduce heterogeneous reaction rates can protect a low-density substrate from severe initial attack, delaying the onset of spallation and limiting mass loss. Design must ensure that coatings do not compromise the thermal protection or generate deleterious particulates themselves.

Design trade-offs, material strategies and mitigation: Lower density is attractive for mass-critical systems; however, the designer must consider increased vulnerability to particle erosion and char spallation at higher chamber pressures. Practical design guidelines and mitigation strategies are summarized as follows: (i) Graded Density Liners: Utilize a low-density facing layer (hot-gas side) for thermal insulation, backed by a medium-to-high-density layer to provide mechanical support and char cohesion. (ii) Local Reinforcement: Integrate ceramic or carbon inserts at predicted particle-impingement hotspots, such as throat entrances and submerged nozzle junctions. (iii) Controlled Filler Fractions: Optimizing the silica filler fraction can reduce resin pyrolysis yield and modify char morphology to resist particle attack, though this must be balanced against increases in thermal conductivity.

Design guidelines and material strategies

(1) Safety margins and “danger zones”

Propulsion designers must recognize the “High Sensitivity Zone” identified in **Figure 2** (densities < 600 $kg \cdot m^{-3}$). In this regime, a small manufacturing deviation in density results in a disproportionately large increase in erosion.

Recommendation: For low-density liners in particle-laden environments, safety margins on insulation thickness should be increased by 1.5× to 2.0× compared to standard high-density components to account for stochastic spallation.

Hybrid Architecture: We recommend a graded design: a high-density, spallation-resistant facing layer (density > 1000 $kg \cdot m^{-3}$) to withstand shear, backed by a low-density layer to minimize thermal soak.

(2) Nanoscale reinforcement

To mitigate the brittleness of low-density chars, recent research suggests

incorporating nanoscale fillers (e.g., carbon nanotubes) to bridge micro-cracks and improve the fracture toughness of the char structure. This approach could effectively lower the brittleness exponent β, expanding the usable envelope of lightweight insulators [31].

8. Open questions and recommended research directions

Future research must bridge the gap between material microstructure and macro-scale erosion through multi-scale investigation (e.g., Nandihalli [31]). More pore-resolved experiments and simulations are required to quantify how permeability and tortuosity change pyrolysis gas dynamics and spallation likelihood under coupled loads, as current pore-scale models lack generalizability [16]. Moreover, systematic matrices that vary density, binder/fiber ratio, and pressure/heat flux together (rather than single-variable tests) will clarify interaction terms that current correlations do not capture through material-process space mapping. Additionally, improved in-motor measurements of particle flux, size distribution, and local impingement momentum are essential to link observed erosion to density-dependent material response, building on NASA's in-motor imaging programs [6]. To enable cross-laboratory comparison, standard high-enthalpy abrasion/ablation test methods with controlled particle seeding are required using standardized test protocols. Finally, researchers should prioritize systematic test matrices that vary density, binder/fiber ratio, and pressure simultaneously to clarify interaction terms, utilizing standardized high-enthalpy abrasion protocols to enable valid cross-laboratory comparisons. Combining pore-scale, mesoscale char evolution and full-motor CFD with particle dynamics remains an active modelling frontier towards multiscale modelling frameworks.

9. Conclusion

The current paper has established that insulation density in silica-phenolic systems is not merely a material property, but a dominant control variable that dictates the transition between energy-limited thermochemical ablation and strength-limited mechanical erosion. By synthesizing historical experimental data with porous media mechanics, we have demonstrated that the traditional trade-off low density for thermal efficiency versus high density for structural durability is governed by non-linear thresholds that become critical under the high-pressure, two-phase flow conditions of modern SRMs.

A primary contribution of this work is the formulation of the Augmented Density-Erosion Equation. Our analysis reveals that standard heat-of-ablation (Q^*) models, while accurate for high-density composites ($\rho > 1400$ kg·m^{-3}), become dangerously non-conservative for low-density felts ($\rho < 600$ kg·m^{-3}). In this low-density regime, the exponential decay of char strength, following Gibson-Ashby cellular mechanics ($\sigma \propto \rho^{1.5}$) renders the material susceptible to catastrophic spallation. The proposed augmented model successfully captures this "spallation gap" by introducing a mechanical penalty term, reconciling the divergence between energetic predictions and the significantly higher recession rates observed in historical firing data.

From a design perspective, these findings suggest that no single density optimum exists for an entire motor. Instead, functionally graded architectures offer the most robust solution: utilizing low-density, high-permeability layers for thermal insulation near the case, shielded by high-density, spallation-resistant liners in regions of high particle momentum (e.g., submerged nozzles and aft domes). Furthermore, the simplified parametric screening proposed herein highlights that safety margins for low-density insulators must be disproportionately larger than those for structural composites to account for stochastic spallation events.

Future qualification efforts must move beyond static torch testing. It is recommended that the adoption of the standardized experimental matrix proposed in Section 5, which explicitly couples heat flux with particle loading and chamber pressure. Ultimately, accurate prediction of SRM insulation behavior requires the integration of the strength-limited erosion physics identified here into coupled multi-physics solvers, ensuring that weight-saving measures do not compromise the structural integrity of the propulsion system.

Funding: This research has no funding source.

Institutional review board statement: Not applicable.

Informed consent statement: Informed consent was obtained from all subjects and their legal guardians involved in the study.

Data availability statement: The data used in this study are available from the corresponding author upon reasonable request.

Conflict of interest: The author declares that he has no conflict of interest.

AI use statement: During the preparation of this work the author used ChatGPT in order to edit and improve the English language quality. After using this tool/service, the author reviewed and edited the content as needed and takes full responsibility for the content of the published article.

References

1. Kim Y, Cho J. Surface erosion analysis for thermal insulation materials of graphite and carbon–carbon composite. Applied Sciences. 2019; 9(16): 3323. doi: 10.3390/app9163323
2. Thakre P, Yang V. Chemical erosion of carbon-carbon/graphite nozzles in solid-propellant rocket motors. Journal of Propulsion and Power. 2008; 24(4): 822–833. doi: 10.2514/1.34946
3. Martin HT, Cortopassi AC, Kuo KK. Assessment of the performance of ablative insulators under realistic solid rocket motor operating conditions. International Journal of Energetic Materials and Chemical Propulsion. 2017; 16(1): 1–22. doi: 10.1615/IntJEnergeticMaterialsChemProp.2017021828
4. Xiao J, Das O, Mensah RA, et al. Ablation behavior studies of charring materials with different thickness and heat flux intensity. Case Studies in Thermal Engineering. 2021; 23: 100814. doi: 10.1016/j.csite.2020.100814
5. Xu YH, Hu X, Yang YX, et al. Dynamic simulation of insulation material ablation process in solid propellant rocket motor. Journal of Aerospace Engineering. 2015; 28(5). doi: 10.1061/(ASCE)AS.1943-5525.0000452
6. McWhorter B, Ewing M, Albrechtsen K, et al. Real-time measurements of aft dome insulation erosion on space shuttle reusable solid rocket motor. In: Proceedings of the 40th AIAA/ASME/SAE/ASEE Joint Propulsion Conference and Exhibit; 11–14 July 2004; Fort Lauderdale, FL, USA. doi: 10.2514/6.2004-3896
7. Nandihalli N, Gorsse S, Kleinke H. Effects of additions of carbon nanotubes on the thermoelectric properties of

$Ni_{0.05}Mo_3Sb_{5.4}Te_{1.6}$. Journal of Solid State Chemistry. 2015; 226: 164–169. doi: 10.1016/j.jssc.2015.02.016
8. Nandihalli N, Mori T, Kleinke H. Effect of addition of SiC and Al_2O_3 refractories on Kapitza resistance of antimonide-telluride. AIP Advances. 2018; 8: 095009. doi: 10.1063/1.5034520
9. Gibson LJ, Ashby MF. Cellular Solids: Structure and Properties, 2nd ed. Cambridge University Press; 1997.
10. Swann RT, Brewer WD, Clark RK. Effect of Composition, Density, and Environment on the Ablative Performance of Phenolic Nylon. NASA TN D-3908. National Aeronautics and Space Administration; 1967.
11. Natali M, Kenny JM, Torre L. Science and technology of polymeric ablative materials for thermal protection systems and propulsion devices: A review. Progress in Materials Science. 2016; 84: 192–275. doi: 10.1016/j.pmatsci.2016.08.003
12. Koo JH, Pilato LA, Wissler GE. Polymer nanostructured materials for propulsion systems. Journal of Spacecraft and Rockets. 2007; 44(6): 1250–1262. doi: 10.2514/1.26295
13. Koo JH, Natali M, Tate J, et al. Polymer nanocomposites as ablative materials—A comprehensive review. International Journal of Energetic Materials and Chemical Propulsion. 2013; 12(2): 119–162. doi: 10.1615/IntJEnergeticMaterialsChemProp.2013005383
14. Turchi A, Bianchi D, Thakre P, et al. Radiation and roughness effects on nozzle thermochemical erosion in solid rocket motors. Journal of Propulsion and Power. 2014; 30(2): 314–324. doi: 10.2514/1.B34997
15. Tompkins S, Kabana W. Effects of Material Composition on the Ablation Performance of Low Density Elastomeric Ablators. NASA TM-X-71932. National Aeronautics and Space Administration; 1973.
16. Zuber C, Reimer T, Esser B, et al. Development of a low-density phenolic-impregnated fibrous ablator. In: Proceedings of the International Conference on Flight vehicles, Aerothermodynamics and Re-entry Missions and Engineering (FAR); 30 September–3 October 2019; Monopoli, Italy.
17. Bianchi D, Nasuti F, Onofri M, et al. Thermochemical erosion analysis for chraphite/carbon-carbon rocket nozzles. Journal of Propulsion and Power. 2011; 27(1): 197–205. doi: 10.2514/1.47754
18. Chinnaraj RK, Kim YC, Choi SM. Thermal behavior of carbon-phenolic/silica phenolic dual-layer ablator specimens through arc-jet tests. Materials. 2023; 16(17): 5929. doi: 10.3390/ma16175929
19. Elwan I, Jabra R, Arafeh MH. Preparation and ablation performance of lightweight phenolic composite material under oxyacetylene torch environment. Journal of Aerospace Technology and Management. 2018; 10: e3118. doi: 10.5028/jatm.v10.935
20. Vaka PR, Rathi N, Ramakrishna PA. Experimental investigation of erosion rate of insulation materials using hybrid rockets. FirePhysChem. 2021; 1(4): 222–230. doi: 10.1016/j.fpc.2021.11.011
21. Uyanna O, Najafi H. Thermal protection systems for space vehicles: A review on technology development, current challenges and future prospects. Acta Astronautica. 2020; 176: 341–356.
22. Mazzaracchio A. One-dimensional thermal analysis model for charring ablative materials. Journal of Aerospace Technology and Management. 2018; 10: e0418. doi: 10.5028/jatm.v10.965
23. Şimşek B, Uslu S. One-dimensional aerodynamic heating and ablation prediction. Journal of Aerospace Engineering. 2019; 32(4): 04019048. doi: 10.1061/(ASCE)AS.1943-5525.0001042
24. Lachaud J, Cozmuta I, Mansour NN. Multiscale approach to ablation modeling of phenolic impregnated carbon ablators. Journal of Spacecraft and Rockets. 2010; 47(6): 910–921. doi: 10.2514/1.42681
25. Chen YK, Milos FS. Ablation and thermal response program for spacecraft heatshield analysis. Journal of Spacecraft and Rockets. 1999; 36(3): 475–483. doi: 10.2514/2.3469
26. Chen G, Xu Y, Zha X, et al. Simulation study of solid rocket motor C/C throat liner ablation based on two regions. Journal of Power and Energy Engineering. 2024; 12(4): 1–19. doi: 10.4236/jpee.2024.124001
27. Gowariker VR. Mechanical and chemical contributions to the erosion rates of graphite throats in rocket motor nozzles. Journal of Spacecraft and Rockets. 1966; 3(10): 1490–1494. doi: 10.2514/3.28682
28. Alanyalioğlu ÇO, Özyörük Y. Conjugate analysis of silica-phenolic charring ablation coupled with interior ballistics. Journal of Propulsion and Power. 2021; 37(4): 528–543. doi: 10.2514/1.B37839
29. Wang L, Li J, Wang Y, et al. Harmonizing lightweight and ablation resistance: Design and performance of multilayer composite insulation materials for solid rocket motors. Polymer Composites. 2025; 46(4): 3427–3438. doi: 10.1002/pc.29183
30. Li Y, Mao C, Wu F, et al. Thermal insulation performance of high-silica/phenolic composites: experimental and numerical study. Composite Structures. 2025; 377: 119855. doi: 10.1016/j.compstruct.2025.119855
31. Nandihalli N. Microwave-driven synthesis and modification of nanocarbons and hybrids in liquid and solid phases. Journal of Energy Storage. 2025; 111: 115315. doi: 10.1016/j.est.2025.115315

32. Sun L, Bao F, Zhang N, et al. Thermo-structural response caused by structure gap and gap design for solid rocket motor nozzles. Energies. 2016; 9(6): 430. doi: 10.3390/en9060430
33. Concio P, Migliorino MT, Nasuti F. Numerical approach for the estimation of throat heat flux in liquid rocket engines. Aerotecnica Missili & Spazio. 2021; 100: 33–38. doi: 10.1007/s42496-020-00060-4
34. Wang L, Tian W, Chen L, et al. Investigation of carbon–carbon nozzle throat erosion in a solid rocket motor under acceleration conditions. International Journal of Aeronautical and Space Sciences. 2021; 22: 42–51. doi: 10.1007/s42405-020-00277-4
35. Tian H, He L, Yu R, et al. Transient investigation of nozzle erosion in a long-time working hybrid rocket motor. Aerospace Science and Technology. 2021; 118: 106978. doi: 10.1016/j.ast.2021.106978
36. Nagler J. On thermoelastic impact modelling of frozen composite target during pre–heated projectile penetration starts of motion. PROOF. 2024; 4: 26–68. doi: 10.37394/232020.2024.4.4
37. Nagler J. Development of a stealth-enabled supersonic interceptor missile: design, propulsion, and guidance. Mechanical Engineering Advances. 2025; 3(3): 3077. doi: 10.59400/mea3077

Appendix A

An approach to evaluate erosion (ablation) rate in protective energy applications (e.g., external or internal (liquid, solid or hybrid) rocket motor (SRM) or spaceship insulations, internal protection in nuclear core, etc.) will be introduced [32–35]. Indeed, the case of ablation concerns material removal or thermochemical phase change (virgin » gas/pyrolysis » char) while the previous section was concerning material deformation. However, since the char state occurs when the threshold temperature is achieved (T_{char}), and hence minimum energy balance between the external thermal gas energy and the material minimum thermal capacity energy until the prescribed threshold char temperature is obtained could be used as follows. In other words, the problem we are trying to solve is what is the maximum distance (x_s) and the minimum time (Δt) for char state formation for a given threshold temperature to rise in order to estimate the optimal erosion rate. It is assumed in the process that the calculation is strict and maintains a linear relationship between the total relative distance of the erosion (material removal) and the speed of the erosion rate through time difference (Δt). In addition, the calculation assumes an overloading region of erosion rate. Accordingly, the classical unsteady transient state energy equilibrium is:

$$m_s C_p \left(T_{char} - T_s\right) = h_c A_s (T_i - T_s)\Delta t, \tag{A1}$$

where the left-hand side term ($mC_p \left(T_{char} - T_s\right)$) represents the resulting thermal energy developed inside the ablative material caused the equilibrium right-hand side term, such as the flowing gas thermal convective energy ($h_c A(T_i - T_s)\Delta t$). The parameters $A_s,\ C_p,\ T_{char}, T_\infty,\ T_i,\ h_c, m_s,\ \Delta t$ represent the shield apparent area for the heat entrance, ablative heat capacity, charred temperature of the protective ablative material, gas surface temperature, the environment initial temperature, the thermal convective coefficient, the ablative protective shield mass and time difference, respectively. Now, by simple algebraic manipulation, Equation (A1) becomes in the following relationship form:

$$\frac{T_{char} - T_s}{T_i - T_s} = \frac{h_c A_s \Delta t}{m_s C_p}. \tag{A2}$$

By substituting $m_s = \rho_s V_s = \rho_s A_s x_s$ and using the erosion rate term $u_s = x_s/\Delta t$ with some algebraic manipulation, yields the expression for the erosion rate speed:

$$u_s = \frac{h_c}{\rho_s C_p} \frac{T_i - T_s}{T_{char} - T_s}, \tag{A3}$$

where $T_i,\ T_{char} < T_s$ and ρ_s, V_s, are the protective shield ablative material specimen density and volume, respectively. In this stage, we will write the convective coefficient parameter as the ratio between the heat flux (q_s) and the temperature

difference ($T_i - T_s$) created over the ablative material external/outer surface, by:

$$h_c = \frac{q_s}{T_s - T_i}. \tag{A4}$$

Substituting relation (A4) back into (A3) gives:

$$u_s = \frac{q_s}{\rho_s C_p \left(T_s - T_{char}\right)}, \tag{A5}$$

and the appropriate total charred erosion distance is:

$$x_s = u_s t_s = \frac{q_s t_s}{\rho_s C_p \left(T_s - T_{char}\right)}, \tag{A6}$$

where t_s is the total heating (e.g., burning) time. Moreover, the more generalized energy case that also considers the heat radiation, turns (A1) into:

$$m_s C_p \left(T_{char} - T_s\right) = h_c A_s \left(T_i - T_s\right) \Delta t + h_r A_s \left(T_i^4 - T_s^4\right) \Delta t \tag{A7}$$

where h_r is the total manipulation between the view factor ($F_{1\to2}$) and the Stefan-Boltzmann constant (σ). After similar algebraic manipulation, the radiative and convective erosion rate will have the following shape:

$$u_{s,convection\ \&\ radation} = \frac{h_c}{\rho_s C_p} \frac{T_i - T_s}{T_{char} - T_s} + \frac{\sigma F_{1\to2}}{\rho_s C_p} \frac{T_i^4 - T_s^4}{T_{char} - T_s}. \tag{A8}$$

Illustratively, empirical evidence shows through distinguisher researches [32–35] that in many burning cases in SRM the heating flux rate fulfills $q_s \approx 5 \left[M \frac{\mathrm{W}}{\mathrm{m}^2}\right]$, using (A4), the convective thermal coefficient is equal to $h_s = 1417.4 \left[\frac{\mathrm{W}}{\mathrm{m}^2\mathrm{K}}\right]$, where T_s = 3550 °C, T_i = 25 °C, respectively. Assuming studies [32–35] that in Carbon–Carbon heat protective insulation shield parameters are T_{char} = 650 °C, ρ_s = 2200 $[\frac{\mathrm{kg}}{\mathrm{m}^3}]$, C_p = 1350 $[\frac{\mathrm{J}}{\mathrm{kgK}}]$, based on Equations (A5) and (A6), the obtained values for the erosion rate and distance are $u_s = 0.58$ [mm/s] and $x_s = 3$ [mm] for total burning time of 5.7 s, which are confirmed by the literature references [34,35] in the overloading erosion region. Suppose we have also radiation involved (from one surface to another only, $F_{1\to2} = 0.1$, $\sigma = 5.67 \cdot 10^{-8}$ [W/(m^{2}K^4)]), the contribution term to the erosion rate will be 0.14 [mm/s] [35] and the total theoretical value is about $u_{s,\ radiation\ and\ convection} = 0.72$ [mm/s]. A useful use for this calculation is also appear in the studies [36,37].